Materials Research. 2014; 17(5): 1238-1250
DOI: http://dx.doi.org/10.1590/1516-1439.268314

Microstructure and Microtexture Assessment of Delamination Phenomena in Charpy Impact Tested Specimens

***Hudison Loch Haskel*[a]*, Ederson Pauletti[a], Juliana de Paula Martins[b], André Luis Moreira de Carvalho[a]**

[a]*Departament of Materials Science and Engineering State, University of Ponta Grossa – UEPG, Ponta Grossa, PR, Brazil*
[b]*Departament of Chemical Engineering, Technology Federal University of Paraná – UTFPR, Curitiba, PR, Brazil*

Received: January 30, 2014; Revised: August 19, 2014

In this article the delamination phenomena, which occurs in the X70 steel during fracture process from the Charpy impact tests, was investigated. Microstructure, microtexture and Taylor factor map analyses were performed by scanning electron microscopy, light microscopy and electron backscatter diffraction, respectively. In a cross-section of two fractured surface regions namely, in the perpendicular and parallel regions to the propagation fracture direction where delamination occurred, it was possible to notice that delamination showed a key role in the anisotropy of impact toughness between the L-T and T-L orientations. The results also revealed that the cause of the delamination can be attributed to the presence of microstructural banding and elongated ferrite grains aligned in a rolling direction. The presence of (100)[011] and (111)[110] crystallographic orientations, with Taylor factors close to 2.7 and 4.5, respectively, were identified in the delamination region. They contribute to the occurrence of cleavage delamination during the fracture process.

Keywords: *EBSD technique, Charpy impact test, microtexture, delamination, API 5L X70 steel*

1. Introduction

The transport of oil and gas through pipelines requires steels that are characterized by a combination of high strength and toughness. These steels are specified by the API 5L standard, and constitute the class of steels known as high strength and low alloy (HSLA). The combination of high strength and toughness allows an increase in the transmission capacity by operation at duct in high pressures. The increase in resistance allows a significant reduction in thickness, with a consequent reduction in weight, and contributes to improving the fracture toughness, which tends to decrease with the thickness increasing[1,2].

The thermomechanical process is mainly responsible for the increasing resistance, and consequently, for the reduction in thickness. However, this procedure can result in anisotropic mechanical properties. This anisotropy is attributed to the presence of inclusions, anisotropic microstructure, crystallographic texture, the presence of inclusions such as manganese sulfide, which tend to become stretched during rolling, and pearlite bands resulting from chemical segregation in the solidification process. With respect to texture, these steels tend to develop a strong fiber texture during controlled rolling, involving deformation, recrystallization and phases transformation[2,3].

With regard to the fracture process by impact test, these steels exhibit the phenomenon known as delamination, whose occurrence can be attributed to crystallographic texture, intergranular fracture along grain boundaries of retained austenite, segregation of elements such as phosphorus and sulfur, microstructural anisotropy, banding, inclusions and aligned particles[3]. Thus many studies have been conducted to determine the relationship between microstructure and mechanical properties, where the technique of electron backscatter diffraction (EBSD) has gained the ability to relate the spatial distribution of plastic deformation with the microstructural characteristics. In addition, this allows a better understanding of the mechanisms responsible for the nucleation and propagation of delamination cracks, which are a major problem in HSLA steels[4,5].

Furthermore many works have investigated the influence of the delamination phenomena on impact toughness of microalloyed HSLA steels[5-9]. Some of these works reported that the presence of delamination can decrease the upper-shelf higher energy in an impact test. Others have reported that the formation of delamination during the fracture process can increase it. Recently, Inoue et al.[7] proposed a new model in which the absorbed energy in the impact test is enhanced by the presence itself. This mechanism is shown in Figure 1, where the formation of two types of delamination can be seen: the crack-arrester type; and the crack-divider type. The first type is formed perpendicular to the direction of fracture propagation, and its formation requires the occurrence of normal planes to the orientation of notch, as the (100) planes and relatively weak interfaces, such as interface grain boundaries, are aligned with the direction of rolling and the interface between the ferritic matrix and cementite particles[10]. In addition, the delamination can be caused by the plastic anisotropy of the banded structure from the controlled rolled steels[11].

*e-mail: hudisonhaskel@hotmail.com

In this context the contribution to the present work was to investigate through the microtexture and Taylor factor analysis in the delamination region, which takes place during fracture process from the Charpy impact tests, the main crystallographic orientations with high and low stored energy can be associated with plastic anisotropy from the banded microstructure of the API 5L X70 steel. These analyses were performed by EBSD technique in two regions of the ductile-brittle transition temperature (DBTT) region; namely, in those perpendicular and parallel to the regions where the delamination occurred. It was also performed to study it in relation to influence of delamination in the anisotropy of impact toughness between the L-T and T-L orientation specimens. Scanning Electron Microscopy (SEM) and Light Microscopy (LM) were also used to understand the mechanisms that produce this phenomenon.

2. Experimental Procedure

2.1. Material

The material used was microalloyed steel, specified as API 5L X70 standard grade, obtained by the thermomechanical treatment of controlled rolling. The chemical composition obtained by optical spectrometry technique is shown in Table 1:

Tensile properties from the L-T and T-L orientations were: 586 (±16.5) MPa and 608 (±21.5) MPa for the ultimate tensile strength, 524 (±21.8) MPa and 538 (±21.7) MPa for the yield limit, and 0.25 and 0.24 strain hardening, respectively. It is possible to see low anisotropy in tensile properties.

2.2. Microstructural characterization

The microstructural characteristics analysis samples were obtained from the rolling direction (RD), transverse to the rolling direction (TD) and normal direction (ND). All samples were ground and polished, with the final polishing step performed with colloidal silica (<1μm). The etching was carried out using a solution of 3% Nital, combined with a solution of 2.4% picral. The observation of the microstructure was performed using an Olympus BX-51 microscope, with a coupled video camera. The capture of images was performed using the IMAGE PRO PLUS 5.1 program. The morphologies of pearlite microconstituent and ferrite phase were investigated by scanning electron microscopy, trademark Shimadzu SSX 550.

2.3. Charpy impact test

Charpy impact tests specimens were removed from the orientation and dimensions. according to ASTM E-23[12], as can be seen in Figure 2.

The tests were carried out in a temperature range of 27°C to –196°C, and the specimens were immersed in a cryogenic bath of nitrogen and anhydrous alcohol liquids for 10 minutes, after which the specimens were tested. To increase the accuracy of this procedure the hammer would only be released if the entire process occurred within 5 seconds.

2.4. Microtexture

Microtexture analysis was performed by EBSD technique. To carry out these measurements two samples were used from the fractured specimens in the L-T orientation, by impact testing at –25 °C with 226J of absorbed energy in the ductile brittle transition temperature region. Analyses were performed in the region perpendicular to the direction of fracture propagation, and near the edges of the crack generated by the crack-divider type of delamination, as shown in Figure 3a). Another analysis was performed parallel to the direction of fracture propagation and near the separation edge caused by delamination, as shown in Figure 3b. The samples were polished in a solution of OP-S (colloidal silica), and then etched with Nital 2%. For EBSD data collection TSL 5 IOM data collection software was used, while OIM Analysis 5 was used for data processing. The scanning electron microscope used to perform such measures was the EDAX TSL EVO MA 10.

3. Results and Discussion

3.1. Microstructural analysis

Figure 4a shows a three-dimensional view of the material microstructure obtained by light microscopy, showing equiaxed ferrite grains (white) and pearlite colonies (black color) forming a banded microstructure, which consists of alternated layers of ferrite and perlite, with similar morphology for both in the rolling and transverse directions.

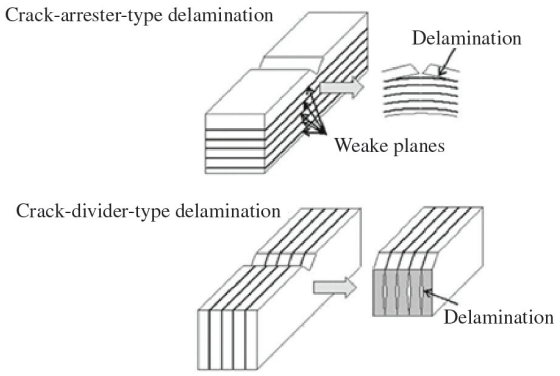

Figure 1. Mechanisms of formation of the delaminations[10].

Table 1. Chemical composition of API X 70 steel.

C	Si	Mn	P	Al	Cu	S
0,14	0,27	1,45	0,01	0,05	0,03	0,00076
Nb	V	Ti	Cr	Ni	Mo	
0,051	0,041	0,018	0,0005	0,001	0,0045	

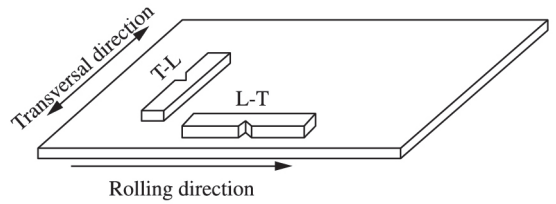

Figure 2. Schematic representation of the orientation notch in directions T-L and L-T for the impact test.

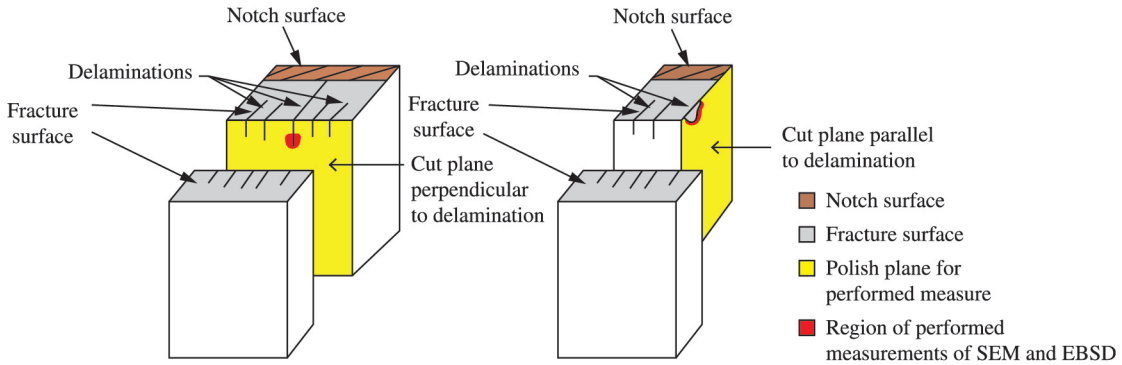

Figure 3. Schematic representation of removed samples for performing EBSD: a) cut plane of the perpendicular direction of fracture propagation; b) cut plane in the parallel region to the direction of fracture propagation.

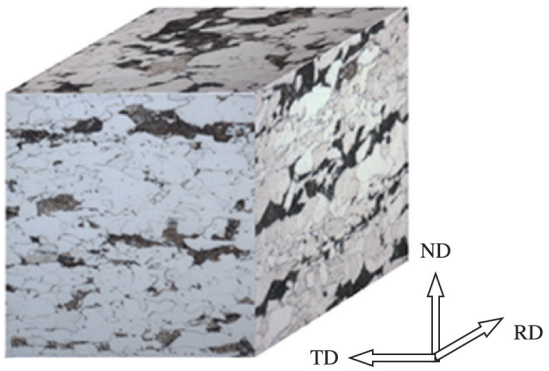

Figure 4. Microstructure from the API X70 steel in 3D dimension.

During the solidification process, some chemical elements, such as manganese, silicon, phosphorus and sulfur, are rejected from the initial formation of ferrite dendrites, resulting in interdendritic regions with a high concentration of solute. The hot rolling in the austenitic phase leads to the formation of regions with a high concentration of solute in a "pancake" shape, which is the basis for the formation of microstructural banding[13]. The manganese chemical segregation during the solidification process, and its scattering in layers during the rolling, has an important role in the formation of banding in HSLA steels. This segregation occurs in interdendritic mode and reduces the carbon activity in the austenite, contributing to carbon segregation surrounding regions rich in manganese. Thus, during the transformation phase after the hot-rolling process, the regions enriched with carbon and manganese are transformed into pearlite[3]. Indeed, chemical analysis reveals that the material exhibits a significant content of manganese (Table 1) in comparison to other alloying elements, which obviously contributes to the formation of banding. This feature of banding induces a difference between plastic and elastic properties of the ferrite and perlite, such as Vickers microhardness values that are approximately 227 and 338 for ferrite and pearlite microconstituents, respectively.

Figures 5a-d display the features of the API X70 steel microstructure obtained by scanning electron microscopy (SEM), using a secondary electron mode. It is possible to notice the characteristics of ferrite and pearlite banding, which are opposite the images obtained by light microscopy: light and dark regions are pearlite and ferrite colonies, respectively. Figure 5a reveals the presence of pearlite colonies with elongated ferrite grains, Figure 5b shows the difference of depth between the ferrite and pearlite, while Figure 5c shows the pearlite lamella formed by ferrite and cementite (Fe_3C), and Figure 5d shows the approximate measures of pearlite interlamellar distance, both slightly above 200nm.

3.2 Charpy impact test

Figure 6a shows the absorbed energy versus the temperature curve for L-T and T-L orientations. It is possible to see that there was a higher scattering in the energy values for the specimens from the L-T orientation when compared to the T-L orientation. In the lower shelf energy where cleavage fracture occurs, both directions provided the same value of energy, 5J. The L-T orientation has a higher upper shelf energy than the T-L orientation. Consequently, this direction has higher absorbed energy for all temperatures, including that relating to the ductile-brittle transition temperature (DBTT). Concerning the DBTT, the L-T orientation also obtained the highest absorbed energy values as a function of orientation, as can be seen in Figure 6b. The DBTT was estimated by comparing the percentage of ductile fracture area, according to specifications of ASTM E-23[12]. Specimens with L-T orientation showed lower range values of DBTT between –38°C and –57°C, while the specimens with T-L orientation exhibited a greater range of DBTT values between –8 °C and –38 °C.

This difference in the increased higher level of energy and the reduction of DBTT can be explained in terms of the ferrite and pearlite band density, and the anisotropic nature of rolled plates.

Studies performed by Shanmugam-Pathak[5] show that if the concentration of bands is greater in the T-L direction, then more weak interfaces are introduced in that direction as a result, which contributes to reducing the DBTT. Although the number of bands per unit area has not been quantified in this study, it is possible to see that such a difference exists, and that it is contributing to the decrease in DBTT for the L-T specimens.

3.3. Feature of fracture and delamination phenomenon

Figure 7 presents an example of a specimen fracture surface from the Charpy impact test with delaminations. In Figure 7a it is possible to observe a crack-arrester type delamination from the specimen tested at –5°C, with 265J of absorbed energy. Figure 7b also shows a set of crack-divider type delaminations from the specimen tested at –36°C, with 100J of absorbed energy.

It can be seen in Figure 7a that the crack-arrester type of delamination occurs perpendicular to the propagation

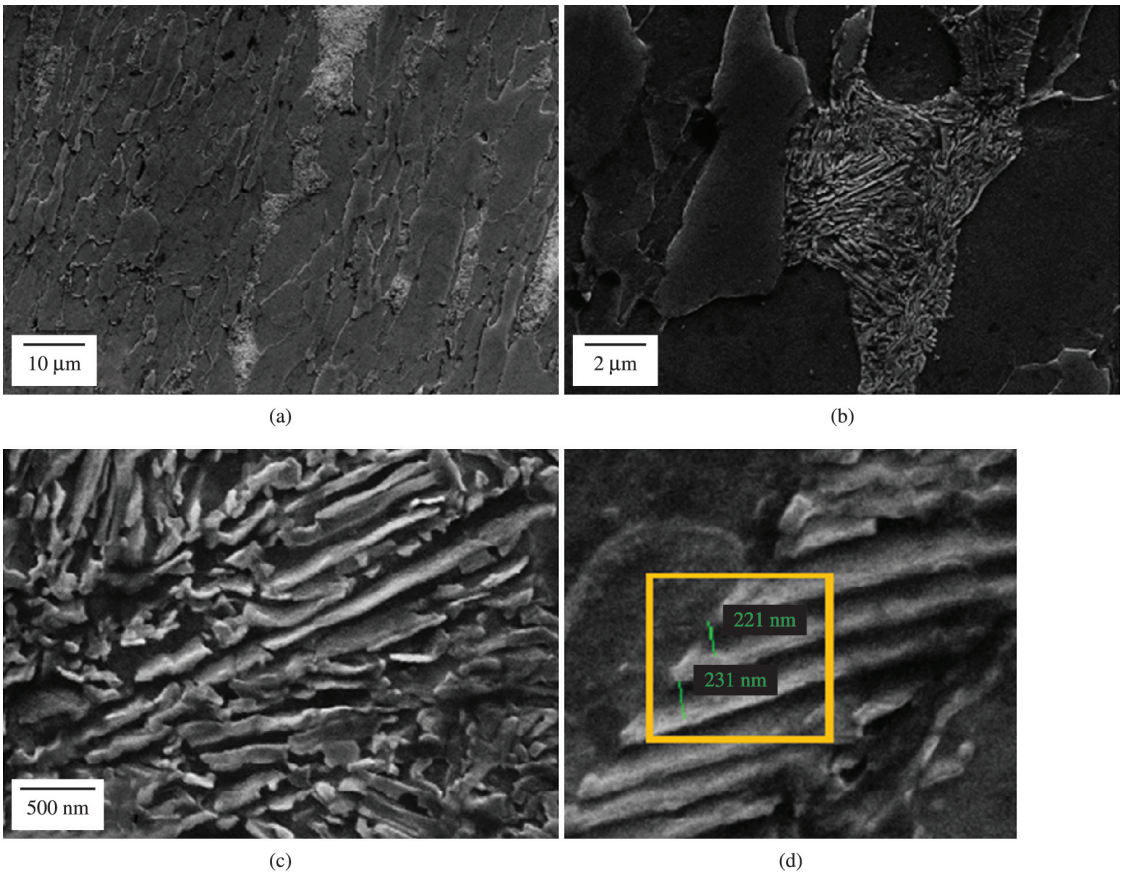

Figure 5. Ferrite and microconstituent pearlite morphology of the X70 steel: a) ferrite and pearlite banding; b) difference of depth between ferrite and pearlite; c) ferrite and cementite lamellae; d) interlamellar distance.

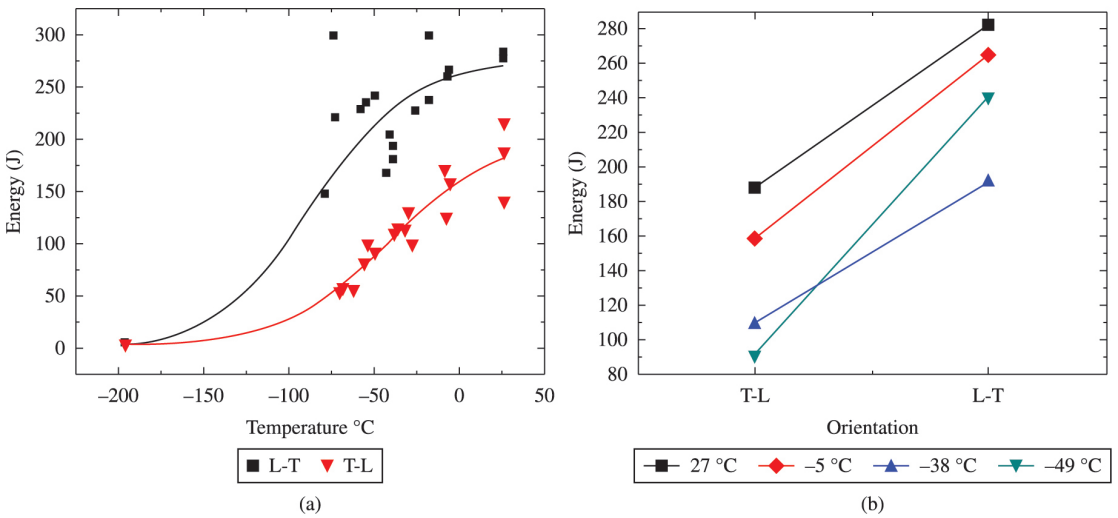

Figure 6. Charpy impact testing: a) as a function of temperature; b) as a function of the orientation (for some temperatures).

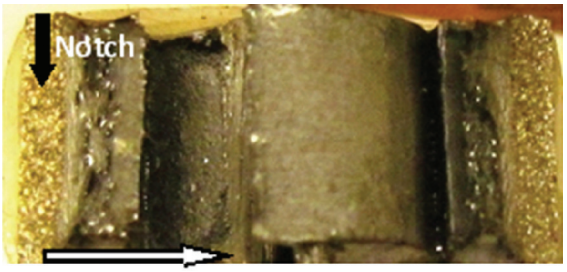

(a)

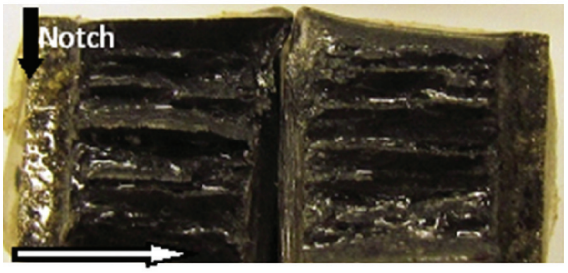

(b)

Figure 7. Fractured surface from the impact test showing the delamination phenomenon: a) crack-arrester type delamination; b) crack-divider type delamination

fracture direction and parallel to the notch, while the crack-divider type of delamination occurs parallel to the propagation fracture direction and perpendicular to the notch. In the present work, the crack-arrester delaminations occur predominantly in the T-L orientation, while crack-divider delaminations occur more frequently in the L-T orientation. In both orientations, the occurrence of delamination took place in the DBTT region. In addition, crack-arrester type delaminations are known for their beneficial effect on increasing upper shelf energy, according to[10]. However, in the present study there was no occurrence of crack-arrester delaminations in the upper shelf energy, for both L-T and T-L orientations.

Moreover, delamination can lead to a reduction in the ductile-brittle transition temperature. This feature can be explained as follow. It is well known that the fracture toughness value depends directly on the stress state at the crack tip, which it increases with decreasing stress triaxiality. Namely, low stress triaxiality induces low plastic constraint at the crack tip, and consequently a higher fracture toughness value. Thus, stress triaxiality can be reduced by relaxing the σ_{zz} stress component (Figure 8) by the occurrence of crack-divider delamination, which takes place perpendicular to the normal direction; that is, the thickness direction. In this case, when delamination takes place, the effective thickness of the samples is reduced, and the σ_{zz} stress decreases to zero at each delamination[5,15].

Accordingly, this reduces the plastic constraint on fracture region and increases the absorbed energy from the Charpy impact test. Moreover, the specimens with

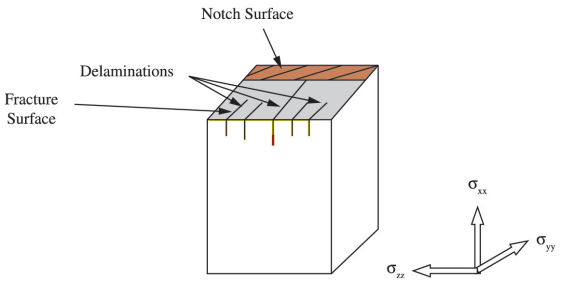

Figure 8. Geometry of a notch with directions of stresses σ_{xx}, σ_{yy}, σ_{zz}.

delamination can act like a cluster of thin samples instead of one thick one. Furthermore, each interface between ferrite and pearlite acts as a weak interface, thus, depending on the density of ferrite-pearlite banding, the delaminations are thinner or thicker[5]. This characteristic can be seen in Figure 9, which shows fractured surfaces from the L-T and T-L orientations, with crack-divider and crack-arrester delaminations. It is possible to notice in Figure 9 that features of delamination differ depending on the orientation specimen. That is, the L-T orientation specimens display the predominance of a central delamination with secondary delaminations, which suggests severe plane stress condition, while the T-L orientation specimens show a predominance of deep, single delamination, thus inducing a low plane stress condition in relation to L-T orientation. This can explain the higher Charpy impact energy, as well as the lower DBTT for the L-T orientation in comparison to the T-L orientation.

For a better understanding of the mechanisms which may be contributing to the formation of delamination, a microstructural analysis by light microscopy was carried out in a perpendicular region to the propagation fracture direction, as shown in Figure 3a. The microstructure analysis close to the edge crack is caused by the crack-divider type delamination, as can be seen in Figure 10. The features that can contribute to the formation of delamination are a banded microstructure and the presence of elongated ferrite grains along delamination, as can be seen in Figures 10a and 10b. The other feature can be associated with incompatibility between the elastic and plastic properties of the ferrite phase and perlite microconstituents, as shown in Figure 10a. This separation between ferrite and pearlite is commonly observed in HSLA microalloyed steels[3,9]. This occurrence of delamination along the grain boundaries indicates that delamination can make small adjustments in its propagation direction, to change from one grain boundary to another[14,15]. Such evidence is displayed in Figure 10c.

However, Figures 11a-c show images obtained by SEM in the secondary electron mode, from the region around a crack generated by delamination of the same sample, used in the analysis of Figure 10. In Figure 11a, the crack propagates along the ferrite, and there is no separation between the ferrite and pearlite in this area. However, as it is a region close to the end of the crack, it cannot be said that such separation does not occur in other regions, such as in the crack initiation region. In Figure 11b a small split can be observed from the A region, shown in Figure 11a. This split suggests some kind of mismatch between interfaces,

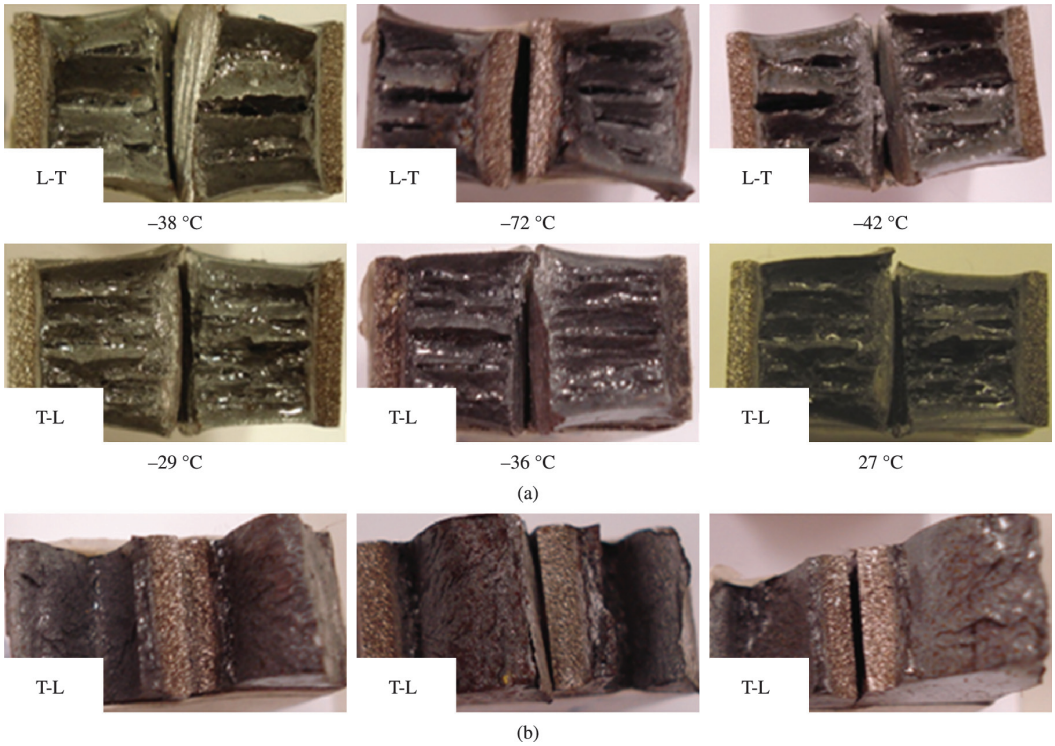

Figure 9. Fractured surfaces from the L-T and T-L orientation showing characteristic of delamination: a) crack-divider type; and b) crack-arrester type.

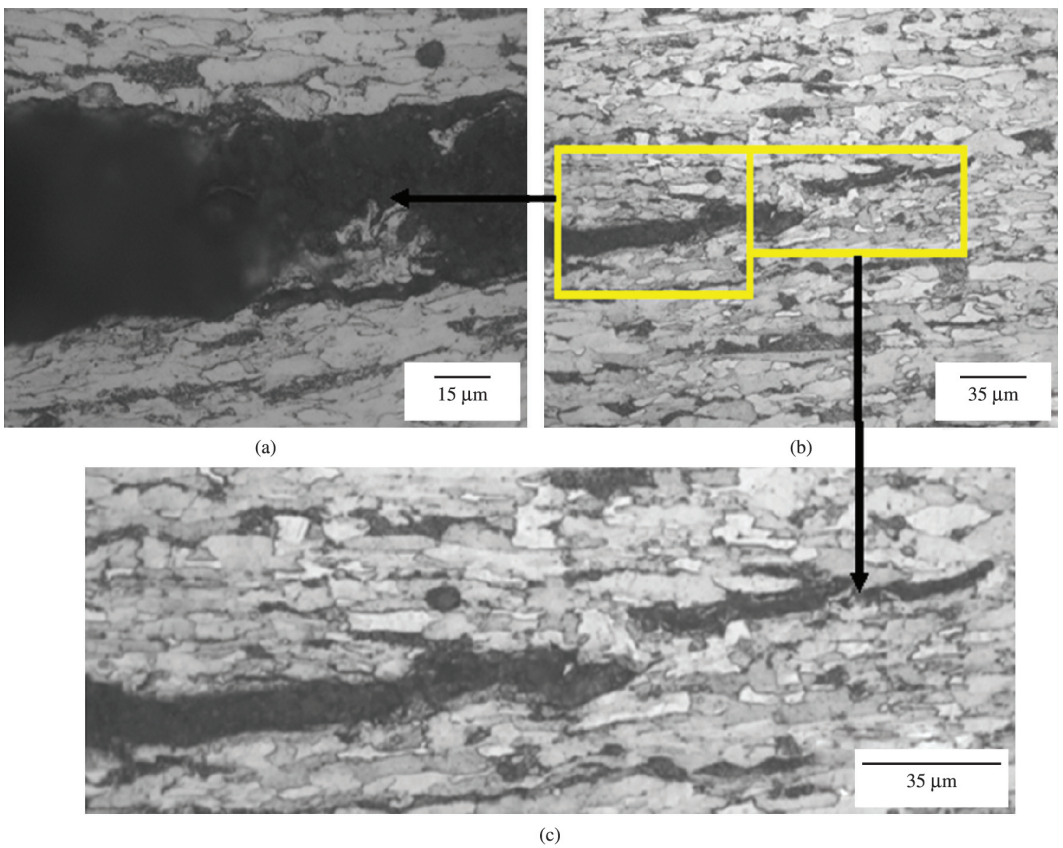

Figure 10. Microstructure of a perpendicular region to the fracture surface: a) separation of ferrite and pearlite; b) crack generated by delamination; c) change direction of crack propagation.

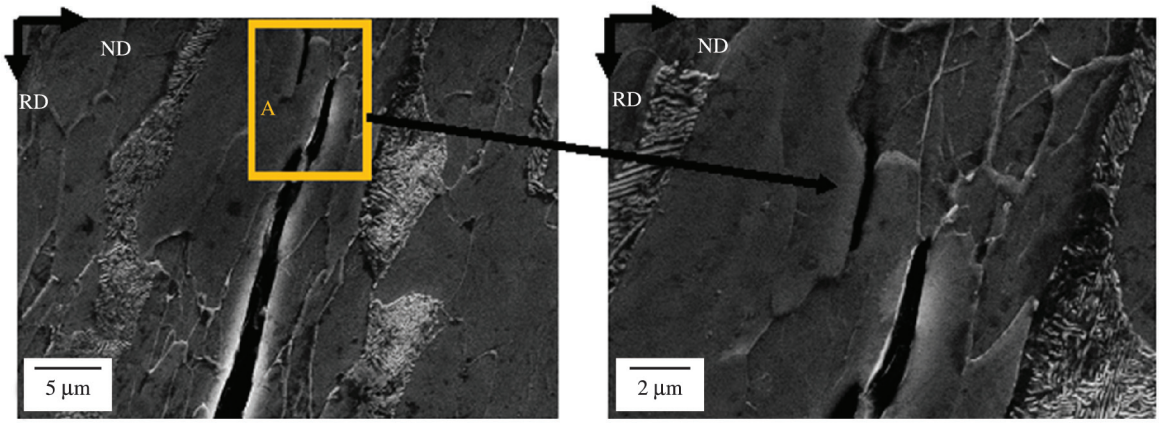

(a) (b)

Figure 11. Microstructure from the around crack region: a) crack propagation along the ferrite; b) fissure observed in the A region.

such as the presence of some inclusion aligned in the rolling direction, or stacking dislocations in the contours of the grain[16].

To identify the fracture micromechanisms that contribute to the formation of delaminations, fractographies were taken, using scanning electron microscopy (SEM) from the impact tested specimen at –53 °C, with 100J of absorbed energy. In Figure 12 a it is possible to notice a ductile fracture type containing delamination.

Figure 12b is a magnification of Figure 12a, which reveals the presence of dimples, originating from the nucleation, coalescence and separation of microvoids during the fracture process. Figure 12c corresponds to the F region, and shows the internal feature of a delamination, with its microdelaminations indicated by arrows. In this figure the presence of brittle fracture can be noted, characterized by a multifaceted surface, that is, cleavage planes, as can be seen in Figure 12d (H region of Figure 12c)). Thus two fracture modes are observed: the brittle fracture within the delamination, indicating some type of decohesion between grain boundary; and the predominance of the ductile fracture region[3].

3.4. Microtexture

To assist in the discussion of the microtexture results, some important orientations observed in rolled materials are shown in Figure 13. These orientations are specified in terms of fiber textures. The cross-section of the Euler space $\Phi 2 = 45°$ was used in the analysis of the orientation distribution function (ODF). The orientations along the RD fiber, also known as α fiber, are developed during hot and cold steel rolling, whereas the TD fiber components also known as ε fiber are more frequent in hot rolled and recrystallized materials, and the ND fiber normal direction or γ fiber is typical rolled ferrite from the low carbon and interstitial-free steels[8].

Figure 14a shows an image obtained by scanning electron microscopy in the propagated crack region by crack-divider type delamination, the orientation distribution map, the inverse pole figure, the orientation distribution function (ODF) for Bunge angle $\Phi_2 = 45°$, and the pole figures of (100) and (110) planes. The quantification of the microtexture was performed by the EBSD technique, using the following parameters: for Figure 14b a step size of 1 micron and 1000 X magnification was used; and for Figure 14c a step size of 3 microns and a magnification of 3000X was used.

In Figure 14b it is possible to see the presence of a dark region, which shows a crack produced by the formation of delamination. The remaining points may be perlite regions, which have very thin lamella (about 200nm), as shown in Figure 5d. As the distance between lamellas is smaller than the step size used, the occurrence to indexation of crystallographic planes to these regions was not possible, resulting in dark regions. Another plausible explanation is associated with the material deformation, which can contribute to the accumulation of dislocations at grain boundaries, resulting in non-indexed regions. In Figure 14b there is a quite heterogeneous grain size distribution, and the absence of (100) planes.

Figure 14c shows the propagated crack region by delamination, and the same propagates along the grain boundary. The occurrence of the delamination along the elongated grain boundaries indicates that it can make minor adjustments in its propagation direction, to change from one grain boundary to another, as shown in Figure 10c. It is confirmed by the separation of grains with [111]||ND and [101]||ND texture components, indicated by 1 up to 5 grains, respectively. It is well known that crack propagation in the grain boundary occurs through high angle boundaries[4,17]. In this context, Figure 15 shows the misorentation angles obtained by EBSD technique, from the scanned region in Figure 13b. For the generation of statistical data points, only disorientation greater than 2° was considered. It is possible to see in Figure 14 that approximately 42% of the misorientation angles among adjacent grains are smaller than 10° (low angle boundaries), while the other 58% are randomly distributed between 10° and 110°, indicating a high grain boundary angle. This means the delaminations appear to propagate by means of a low energy fracture mechanism, which is the same as with the absence of (100) planes, as can be seen in Figure 14c.

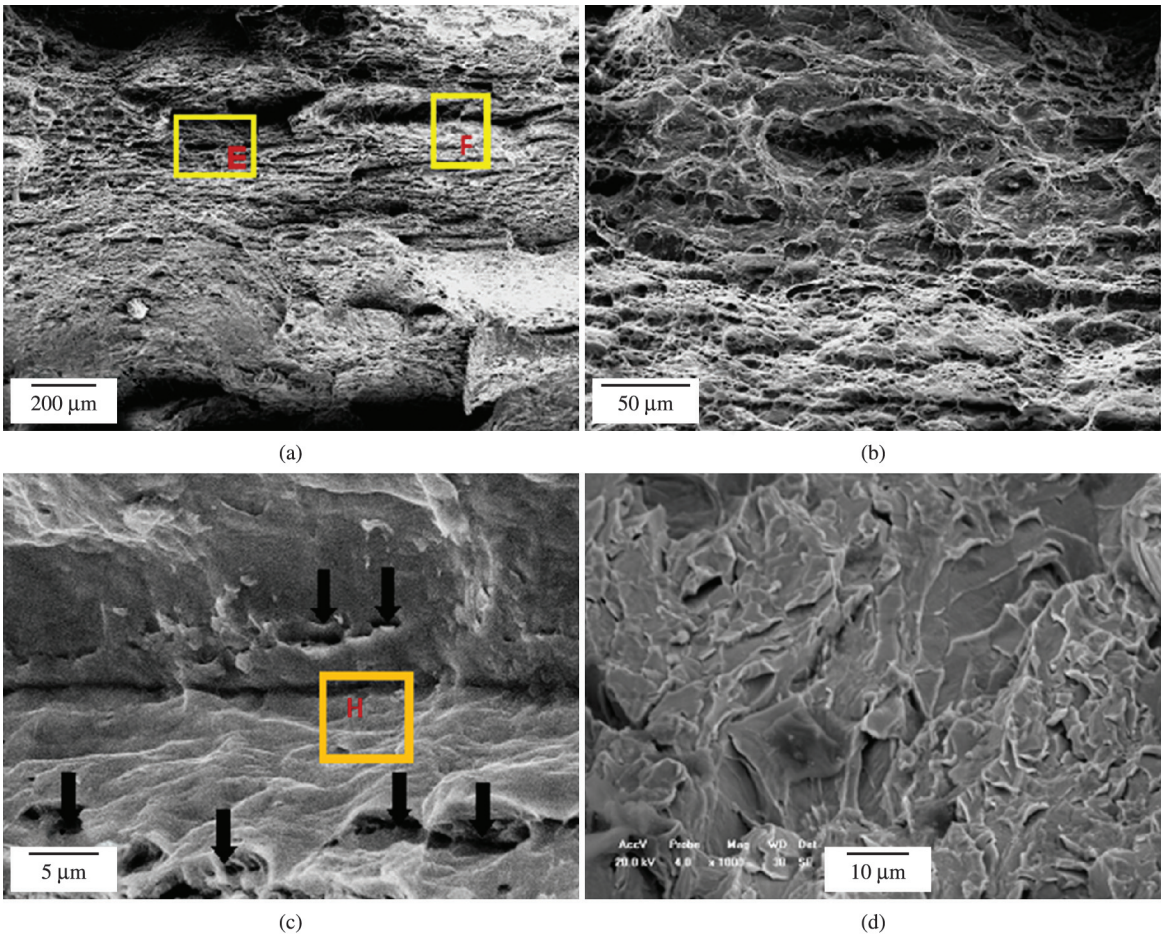

Figure 12. Fractographics by SEM, of specimen Charpy impact testing: a) delamination aspects; b) region shown in E; c) region F (inside delamination); d) region H (in the "walls" of delamination).

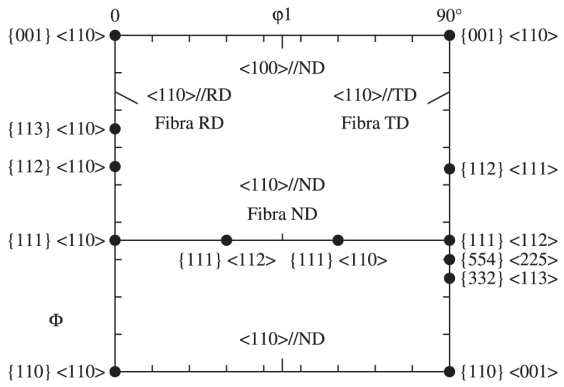

Figure 13. ODF section with Φ2 = 45 ° showing the position of the major components of texture along the RD, TD and ND fibers.

To quantify the major components involved from the delamination region, the pole figures and ODF were generated, as shown in Figures 14d and e. Both used the orientation map from Figure 14b, which provides better precision in the information owing to its higher scanned area. The ODF shown in Figure 14d reveals that the orientations have α fiber components, which are typical components from the deformed ferrite. With the use of the ODF section shown in Figure 13, it was possible to index the ODF main components, namely: (221)[1$\bar{1}$0], (223)[1$\bar{1}$0], (112)[1$\bar{3}\bar{2}$] and (332)[023]. Pole figures shown in Figure 14e confirm the presence of the α fiber components identified by the ODF.

Furthermore, crystallographic plane materials, with (100) orientation aligned in the rolling direction, show a strong tendency to occur cleavage fracture during impact test[3,4,6-9,14]. To identify whether the separation of the (100) planes occurred in this case, the microtexture on the edge of the parallel section's (Figure 3b)) fractured surface was measured, where the delamination was generated. This sample was the same used in the analysis of Figure 14, but using step size of 1 micron and 1000X magnification. The results obtained are displayed in Figure 16. It can be observed in Figure 16a the difference of depth between the ferrite and pearlite, while Figure 16b shows the distribution orientation map, where there is a heterogeneous distribution of grain sizes, and a few areas where there were no indexing of the planes, and the presence of (100) planes. The ODF to Bunge angle Φ_2 = 45° is shown in Figure 16c, and its indexing shows the main texture components are (223) [0$\bar{3}$2] and (332) [1$\bar{1}$0].

The pole figures are shown in Figure 16d, where the greatest occurrence in the (111) center plane is noted, and the indexing of some components reveals the presence of (100)[011] and (111)[110] orientations. The occurrence of delaminations is often attributed to the presence of plastic anisotropy of the banded structures, typically found in controlled rolling steels. In this context, the grains in deformed bands are composed of two families, which can be broadly classified into (111)[110] and (100)[011] types. Under applied stress, the different textures bands are expected to behave differently, thus producing a discontinuity in plastic strain at the boundaries of the bands, which ultimately leads to fracture along the grain boundary. However, some studies have found that the

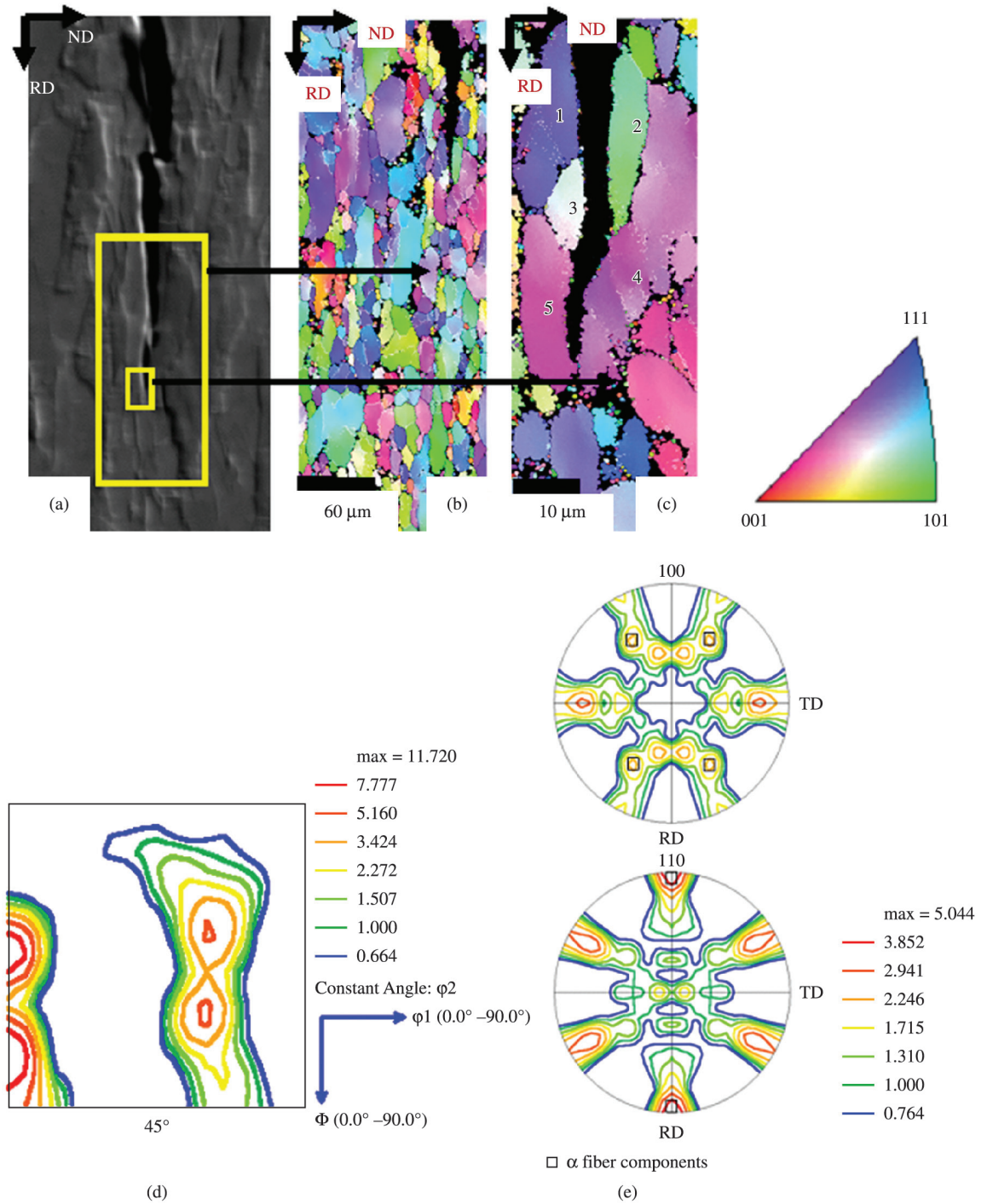

Figure 14. Microtexture from the vicinity delamination region: a) analyzed region by EBSD; b) and c) orientation distribution map; d) orientation distribution function; and e) pole figures.

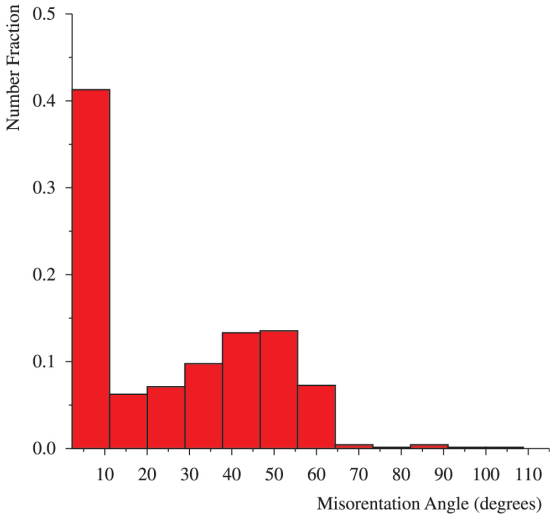

Figure 15. Misorientation angles between adjacent grains near to edges of delamination.

plastic anisotropy between the (100)[011] and (111)[110] orientations are not sufficient to cause delamination. Thus, some works suggest that delamination is a cleavage fracture, when the same fracture is initiated from the perlite colonies, when such colonies are surrounded by deformed ferrite grains, with orientation close to (100)[011]. In this case, the crack will propagate rapidly within these regions, causing delamination[18].

However, in the present study, both features were found: namely, the presence of (100)[011] and (111)[110] orientations, identified in the pole figure for the (100) plane and brittle fracture, caused by delamination, as shown in Figures 16d, 12c and 12d, respectively. This suggests that both factors contribute to the formation of the crack-divider type of delamination.

As seen in Figure 14c, the nucleated crack by delamination separated the grains with (111)||ND and (101)||ND texture components. It is evident that, in this case, the presence of the (111)||ND components near to the delamination should be noticed, thus confirming the separation of ferrite planes. Besides, the presence of the (100) planes was also confirmed. However, as in this

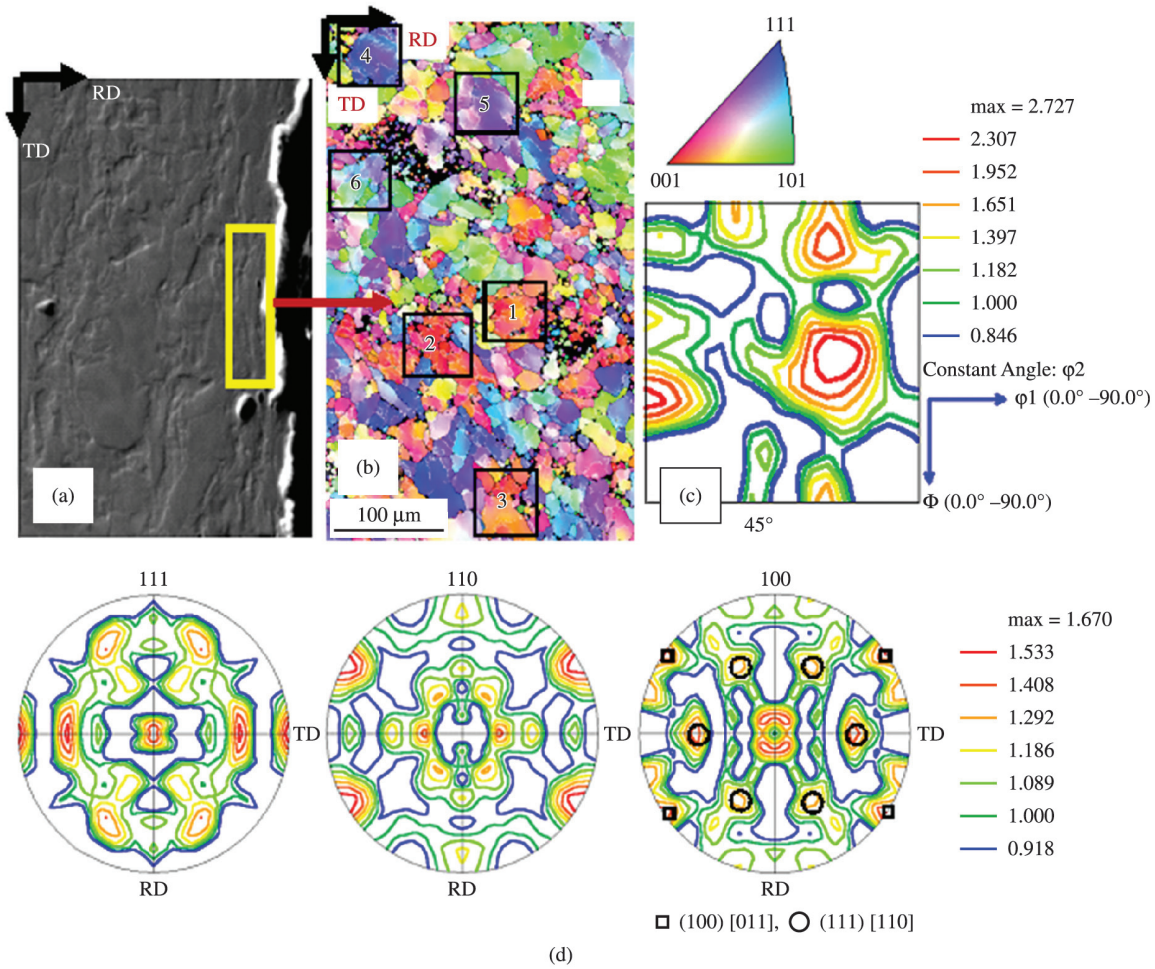

Figure 16. Orientation distributions map: a) SEM scanned region; b) orientation distribution maps, magnification of 1000X; c) orientation distribution function; d) pole figures.

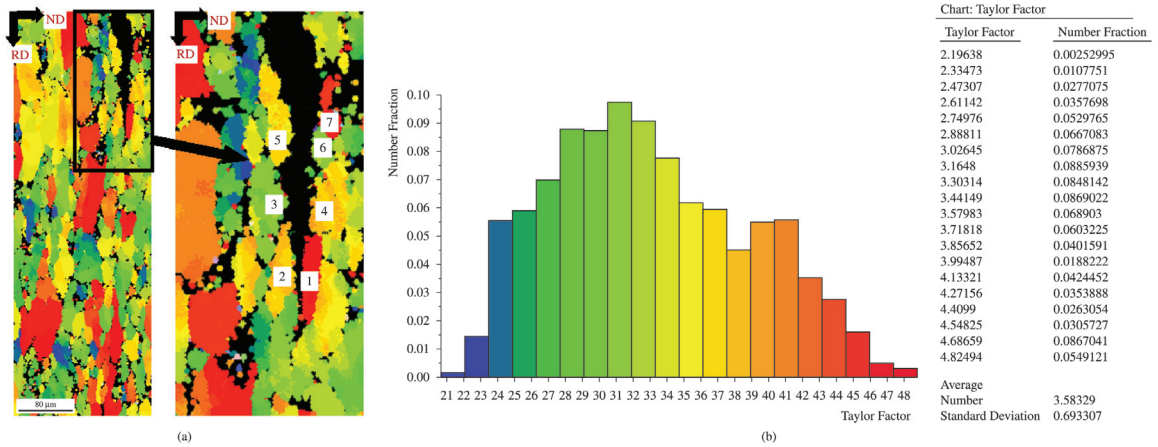

Chart: Taylor Factor

Taylor Factor	Number Fraction
2.19638	0.00252995
2.33473	0.0107751
2.47307	0.0277075
2.61142	0.0357698
2.74976	0.0529765
2.88811	0.0667083
3.02645	0.0786875
3.1648	0.0885939
3.30314	0.0848142
3.44149	0.0869022
3.57983	0.068903
3.71818	0.0603225
3.85652	0.0401591
3.99487	0.0188222
4.13321	0.0424452
4.27156	0.0353888
4.4099	0.0263054
4.54825	0.0305727
4.68659	0.0867041
4.82494	0.0549121
Average	
Number	3.58329
Standard Deviation	0.693307

Figure 17. Taylor factor map: a) scan region; b) histogram of number fractions.

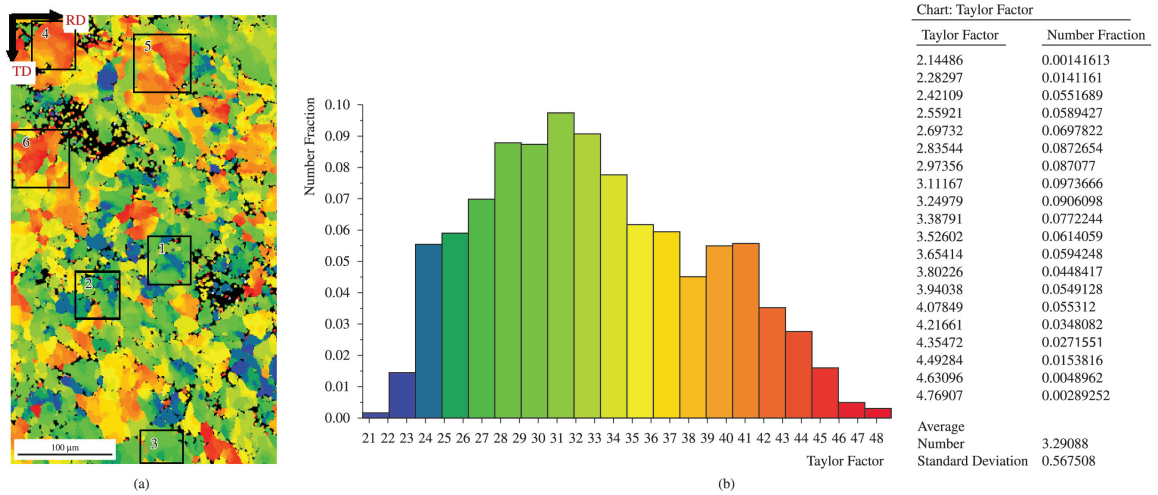

Chart: Taylor Factor

Taylor Factor	Number Fraction
2.14486	0.00141613
2.28297	0.0141161
2.42109	0.0551689
2.55921	0.0589427
2.69732	0.0697822
2.83544	0.0872654
2.97356	0.087077
3.11167	0.0973666
3.24979	0.0906098
3.38791	0.0772244
3.52602	0.0614059
3.65414	0.0594248
3.80226	0.0448417
3.94038	0.0549128
4.07849	0.055312
4.21661	0.0348082
4.35472	0.0271551
4.49284	0.0153816
4.63096	0.0048962
4.76907	0.00289252
Average	
Number	3.29088
Standard Deviation	0.567508

Figure 18. Mapping of Taylor factor: a) scan region; b) histogram of number fractions.

case, only the microtexture was analyzed, and it cannot confirm whether this is a general rule for the nucleation of delamination in the material under study.

Experimentally, it is well known that the stored energy during the deformation changes with the crystallographic orientation of the grains. The Taylor factor is a parameter that correlates to macroscopic deformation behavior, with microstructural characteristics of the material[19]. According to the theory of plasticity, the stored energy increases with the Taylor factor, which in turn, depends on the crystallographic orientation grain in relation to the direction of applied stress. The Taylor factor is defined as:

$$M = \sum \delta\gamma_i / \delta\varepsilon \quad (1)$$

where $\delta\gamma_i$ represents shear portions in each of the activated sliding systems in a certain grain, while the sample receives a macroscopic deformation $\delta\varepsilon$.

Thus, measures of the Taylor factor mapping were performed from the delamination regions, to identify crystallographic orientations with high and low stored energy, which can be associated to plastic anisotropy from the banded microstructure shown in Figure 10, as well as the main texture components associated with this behavior, as shown in Figures 14 and 16.

Figure 17 shows the Taylor factor mapping from the delamination proximity (Figures 14 b and c)). It is possible to note in Figure 17b that the separation generated by delamination has occurred among grains with a different Taylor factor. The 1 and 2 grains were separated with a Taylor factor of around 4.8 and 3.5, respectively. In others words, it means that cracks spread among grains with high and low energy. The same situation took place for the 5 and 7 grains. The 3 and 4 grains also show a Taylor factor in the range of 3.0 and 3.6, and the same occurred with the 5 and 6 grains. This difference of Taylor factor among neighboring grains generates strong incompatibilities in the process of plastic deformation, favoring the fracture along the grain boundaries from the crack-divider delamination, as can be observed in Figure 17.

It notes that close to 57% of grains have a Taylor factor between 2.9 and 3.6, and 27.61% of grains have a Taylor factor between 4.1 and 4.8. In addition, the 4 and 5 grains

show a difference of tonality; that is, different (slightly darker regions) material regions experienced greater deformation, thus higher Taylor Factor was obtained, while clearer region suffered less deformation and consequently had a lower Taylor factor.

Figure 18 shows the Taylor factor mapping from the sample region shown in Figure 16b. In this case it was observed that approximately 55.34% of the grains have Taylor factors between 2.7 and 3.4, while 14.01% of the grains have a Taylor factor between 4.07 and 4.76. Thus, this sample presented a lower number of fractions of grains with Taylor factors between 4.1 and 4.8, when compared with the sample analyzed in Figure 17, that shows a minor absorbed energy in this region once the Taylor factor map refers to the local energy stored[18].

The stored energy from the low carbon steels can be different according to the sequence: $E_{(110)} > E_{(111)} > E_{(211)} > E_{(100)}$, where *hkl* plans refer to rolling plans in each grain[20]. Thus a comparison can be performed from the 1, 2 and 3 numbered regions of Figures 16b and 18a, where the presence of the (100) planes and Taylor factor close to 2.7 can be observed in the respective regions. Consequently, a smaller stored energy was absorbed. However, the 4, 5 and 6 numbered regions of the same figures show a predominance of the (111) planes and a higher Taylor factor close to 4.5.

4. Conclusions

The features of delamination regions were investigated, using EBSD technique, LM and SEM analyses in Charpy impact specimens made of X70 steel. The results can be drawn as follows:

Charpy impact testing from the API 5L X70 steel shown during the fracture process takes place in two types of delaminations the crack-arrester and crack-divider and both occur in the DBTT region.

The crack-divider type had a predominance of central and secondary delaminations, whereas the crack-arrester showed a predominance of deep, single delamination. It was possible to notice that delamination played a key role in the anisotropy of impact toughness between the L-T and T-L orientations.

The results from the LM, SEM and microtexture revealed that the cause of the delamination can be attributed to the presence of microstructural banding and elongated ferrite grains, aligned in the rolling direction. The presence of (100)[011] and (111)[110] crystallographic orientations was identified in the delamination region, with Taylor factors close to 2.7 and 4.5, respectively.

This suggests the difference of stored energy from the planes produces a strong mismatch in Taylor factors, and contributes to an increase in the plastic anisotropy among regions of planes, and consequently, the occurrence of cleavage delamination during the fracture process.

The main microtexture components obtained from the perpendicular region of delamination from ODF were (221)[$1\bar{1}0$], (223)[$1\bar{1}0$], (112)[$1\bar{3}\bar{2}$] and (332)[023] orientations, while in the parallel region they were (223)[$0\bar{3}\bar{2}$] and (332)[$1\bar{1}0$] orientations. Both orientations are typical components of the deformed ferrite.

Acknowledgments

The authors would like to thank the USIMINAS for providing the material under study, the UFF-Federal Fluminense University, for performing the EBSD measurements, and CAPES for providing a scholarship and the project (Case No. PNPD-23038.008242/2010-08)

References

1. Guo W, Dong H, Lu M and Zhao X. The coupled effects of thickness and delamination on cracking resistance of X70 pipeline steel. *International Journal of Pressure Vessels and Piping*. 2002; 79(6):403-412. http://dx.doi.org/10.1016/S0308-0161(02)00039-X.
2. Venkatsurya PKC, Jia Z, Misra RDK, Mulholland MD, Manohar M and Hartmann JE Jr. Understanding mechanical property anisotropy in high strength niobium-microalloyed linepipe steels. *Materials Science and Engineering A*. 2012; 556:194-210. http://dx.doi.org/10.1016/j.msea.2012.06.078.
3. Joo MS, Suh DW, Bae JH and Bhadeshia HKDH. Role of delamination and crystallography on anisotropy of Charpy toughness in API-X80 steel. *Materials Science and Engineering A*. 2012; 546:314-322. http://dx.doi.org/10.1016/j.msea.2012.03.079.
4. Yu H. Influences of microstructure and texture on crack propagation path of X70 acicular ferrite pipeline steel. *Journal of University of Science and Technology Beijing*. 2008; 15(6):683-687. http://dx.doi.org/10.1016/S1005-8850(08)60271-6.
5. Shanmugam P and Pathak SD. Some studies on the impact behavior of banded microalloyed steel. *Engineering Fracture Mechanics*. 1996; 53(6):991-1005. http://dx.doi.org/10.1016/0013-7944(95)00159-X.
6. Yan W, Sha W, Zhu L, Wang W, Shan YY and Yang K. Delamination fracture related to tempering in a high-strength low-alloy steel. *Metallurgical and Materials Transactions. A, Physical Metallurgy and Materials Science*. 2010; 41(1):159-171. http://dx.doi.org/10.1007/s11661-009-0068-y.
7. Inoue T, Yin F, Kimura Y, Tsuzaki K and Ochiai S. Delamination effect on impact properties of ultrafine-grained low carbon steel processed by warm caliber rolling. *Metallurgical and Materials Transactions. A, Physical Metallurgy and Materials Science*. 2010; 41(2):341-355. http://dx.doi.org/10.1007/s11661-009-0093-x.
8. Baczynski GJ, Jonas JJ and Collins LE. The influence of rolling practice on notch toughness and texture development in high-strength linepipe. *Metallurgical and Materials Transactions. A, Physical Metallurgy and Materials Science*. 1999; 30(12):3045-3054. http://dx.doi.org/10.1007/s11661-999-0215-5.
9. Verdeja JI, Asensio J and Pero-Sanz JA. Texture, formability, lamellar tearing and HIC susceptibility of ferritic and low carbon steels. *Materials Characterization*. 2003; 50(1):81-86. http://dx.doi.org/10.1016/S1044-5803(03)00106-2.

10. Jafari M, Kimura J and Tsuzaki K. Enhancement of upper shelf energy through delamination fracture in 0,05 pct P doped High Strength steel. *Metallurgical and Materials Transactions. A, Physical Metallurgy and Materials Science*. 2012; 43(7):2453-2465. http://dx.doi.org/10.1007/s11661-012-1095-7.
11. Chao HC. Mechanism of anisotropic lamellar fractures. *Metallurgical and Materials Transactions. A, Physical Metallurgy and Materials Science*. 1978; 9(4):509-514. http://dx.doi.org/10.1007/BF02646407.
12. American Society for Testing and Materials – ASTM. *ASTM Standard E23*. ASTM; 2002.
13. Thompson SW and Howell PR. Factors influencing ferrite/perlite banding and origin of large pearlite nodules in a hypo eutectoid plate steel. *Materials Science and Technology*. 1992; 8(9):777-784. http://dx.doi.org/10.1179/mst.1992.8.9.777.
14. Jian H, Jiang F, Wei L, Zheng X and Wen K. Crystallographic mechanism for crack propagation in the T7451 Al-Zn-Mg-Cu alloy. *Materials Science and Engineering A*. 2010; 527(21-22):5879-5882. http://dx.doi.org/10.1016/j.msea.2010.05.063.
15. Song R, Ponge D and Raabe D. Mechanical properties of an ultrafine grained C-Mn steel processed by warm deformation an annealing. *Acta Materialia*. 2005; 53(18):4881-4892. http://dx.doi.org/10.1016/j.actamat.2005.07.009.
16. Honeycombre RWK. *Aços Microestrutura e Propriedades*. 1st ed. Edward Arnold; 1985
17. Wright SI and Field DP. Recent studies of local texture and its influence on failure. *Materials Science and Engineering A*. 1998; 257(1):165-170. http://dx.doi.org/10.1016/S0921-5093(98)00835-1.
18. Ray RK and Jonas JJ. Transformations texture in steels. *International Materials Reviews*. 1990; 35(1):1-36. http://dx.doi.org/10.1179/095066090790324046.
19. Yin F, Hanamura T, Inoue T and Nagai K. Fiber Texture and Substructural features in the caliber-rolled low-carbon steels. *Physical Metallurgy and Materials Science*. 2004; 35(2):665-677. http://dx.doi.org/10.1007/s11661-004-0378-z.
20. Humphreys FJ and Hatherly M. *Recrystallization and Related Annealing Phenomena*. 2nd ed. Amsterdam: Elsevier; 2004.